Heliyon 11 (2025) e41276

Contents lists available at ScienceDirect

Heliyon

journal homepage: www.cell.com/heliyon

Research article

Influence of cobalt substitution in $CoFe_2O_4$ nanoparticles on structural, morphological, cation distribution, optical and magnetic properties

Z. Mosleh [a,*], M. Beygmohammadvand [a], A. Ghotbi Varzaneh [a,b], P. Kameli [a]

[a] Department of Physics, Isfahan University of Technology, Isfahan 84156-83111, Iran
[b] Institute of Microstructure Technology, Karlsruhe Institute of Technology, Karlsruhe, 76344, Germany

ARTICLE INFO

Keywords:
Spinel ferrites
Cation distribution
Optical band gap
Saturation magnetization

ABSTRACT

This paper presents the first-time synthesis of $CoFe_{2-x}Co_xO_4$ nanoparticles (where x = 0.0, 0.1, 0.2, 0.3, 0.4, 0.5, and 0.6) through hydrothermal methods utilizing metal chloride precursors. X-ray diffraction (XRD) analysis confirms the formation of a cubic spinel structure characterized by the $Fd\bar{3}m$ space group. Field Emission Scanning Electron Microscopy (FE-SEM) images reveal that the average grain size of the nanoparticles lies between 50 nm and 90 nm. Notably, the optical band gap of the Co^{3+}-doped samples exhibits a gradual increase from 1.7 eV to 2.5 eV. Furthermore, a reduction in saturation magnetization was noted with increasing doping content at both 5 K and 300 K. The observed decrease in saturation magnetization in the doped samples can be attributed to the migration of Co^{2+} ions from the B site to the A site, as well as the substitution of Fe^{3+} ions with Co^{3+} ions in the B site. Additionally, the influence of annealing temperature on the structure, morphology, and magnetic properties of the nanoparticles was examined.

1. Introduction

Magnetic nanoparticles have garnered significant attention over the past few decades due to their potential applications in various fields, including magnetic recording, magnetic resonance imaging, medicine, data storage, solar cells, sensors, and catalysis [1–6]. The optical properties of $CoFe_2O_4$ nanoparticles have attracted researchers because they are useful for optical data storage devices. $CoFe_2O_4$ nanoparticles exhibit strong magneto-optical effects [7]. Also, the absorption and transmission spectra of $CoFe_2O_4$ nanoparticles are influenced by their size, shape, and crystal structure. These properties can be tailored to control the optical response of the nanoparticles for specific applications, such as optical filters and colorants [8]. $CoFe_2O_4$ nanoparticles have been shown to exhibit nonlinear optical properties, such as second harmonic generation and two-photon absorption. These properties make them attractive for applications in optical communications and laser technology [9].

Spinel ferrites, a prominent class of magnetic materials, possess a cubic structure with the general formula AB_2O_4, where A and B represent different metal cations situated at two specific sites: A (tetrahedral) and B (octahedral). Each crystallographic unit cell contains eight formula units of AB_2O_4, leading to 64 A sites (of which 8 are occupied) and 32 B sites (with 16 occupied). The arrangement of metal cation M^{2+} within the spinel structure allows for categorization into normal, inverse, and mixed spinel. In a normal spinel configuration, A^{2+} cations occupy only the tetrahedral sites, while B^{3+} ions are found exclusively in the octahedral

* Corresponding author.
E-mail address: z.mosleh@ph.iut.ac.ir (Z. Mosleh).

https://doi.org/10.1016/j.heliyon.2024.e41276
Received 15 August 2024; Received in revised form 10 November 2024; Accepted 15 December 2024

Available online 30 December 2024
2405-8440/© 2024 The Author(s). Published by Elsevier Ltd. This is an open access article under the CC BY-NC-ND license (http://creativecommons.org/licenses/by-nc-nd/4.0/).

sites. Conversely, in inverse spinel structures, all A cations and half of the B cations occupy octahedral sites, while the remaining B cations are located in tetrahedral sites. Mixed spinel structures represent a further variation, where both metal cations and B^{3+} ions are distributed across octahedral and tetrahedral sites, with an inversion parameter indicating the degree of inversion [10,11].

Various synthesis methods have been employed to produce spinel ferrites, including solid-state reaction techniques [12], sol-gel auto-combustion [13], and hydrothermal methods [14]. Among the range of spinel ferrite nanoparticles, cobalt ferrite ($CoFe_2O_4$) has attracted considerable interest due to its inverse spinel structure and superior electromagnetic properties. $CoFe_2O_4$ offers high coercivity, significant magnetization, excellent chemical stability, mechanical hardness, and notable cubic magnetocrystalline anisotropy [15]. These attributes make cobalt ferrite a prime candidate for diverse applications in the field of magnetism and materials science.

The properties of $CoFe_2O_4$ ferrite are significantly influenced by the size and shape of its nanoparticles, which are determined by both the preparation method and the type of substituent used. In this study, we employed the hydrothermal method to synthesize nanoscale ferrites. This approach offers distinct advantages in terms of controlling grain size, crystalline phase, particle morphology, and reaction temperature. The hydrothermal technique allows for the formation of nanomaterials across a wide temperature range, from room temperature to elevated temperatures. Furthermore, the morphology of the synthesized materials can be tailored by utilizing low-pressure or high-pressure conditions, based on the vapor pressure of the primary reactants involved in the reaction. In addition, the magnetic properties of spinel ferrites can be modified by adjusting their chemical composition, for example, by incorporating transition metals.

This paper is motivated by the need to enhance the properties of cobalt ferrite through controlled doping with cobalt ions. By synthesizing $CoFe_{2-x}Co_xO_4$ nanoparticles using a hydrothermal method, we aim to investigate the effects of varying cobalt concentrations on the structural, magnetic, and optical properties of the nanoparticles. The systematic study of these properties is vital for understanding how ion substitution and migration can influence magnetization, which is essential for optimizing materials for specific applications. By examining the relationship between doping concentration, grain size, optical band gap, and thermal effects via annealing, this research contributes to a deeper understanding of the interplay between composition and properties in magnetic nanoparticles.

2. Experimental

2.1. Synthesis procedure

To synthesize the nanocrystalline powders of $CoFe_{2-x}Co_xO_4$ (where x = 0.0, 0.1, 0.2, 0.3, 0.4, 0.5, and 0.6), we utilized a hydrothermal method. The starting materials included high-purity ferric chloride hexahydrate ($FeCl_3.6H_2O$), cobalt chloride hexahydrate ($CoCl_2.6H_2O$), and sodium hydroxide (NaOH). Initially, stoichiometric amounts of the metal chlorides were dissolved in 28 mL of distilled water to form a homogeneous solution. A NaOH solution was prepared by dissolving 1 g of NaOH in 50 mL of distilled water and then adding it and then added dropwise to the chloride solution while stirring vigorously. Following this, the mixture was stirred magnetically for 1 hour before being transferred into an autoclave. The solution was heated to 250 °C and maintained at that temperature for 2 hours, after which it was allowed to cool to room temperature. The resulting precipitate was washed several times with water and ethanol sequentially before being dried at 60 °C for 6 hours to obtain the final nanocrystalline powders.

2.2. Characterizations

The synthesized samples were characterized for their crystal structure using X-ray diffraction (XRD) patterns with CuKα radiation (λ = 0.15406 nm). The morphology and size of the nanoparticles were assessed via field emission scanning electron microscopy (FE-SEM). Optical absorption spectra were collected using a Perkin Elmer UV–Vis spectrophotometer over the wavelength range of 190 to 1100 nm, with a scan interval of 0.1 nm. The ferrite powder sample was dispersed in ethanol. A small quantity of the sample suspension was then transferred to a cuvette, which is subsequently positioned in the sample holder of the UV-Vis spectrophotometer. The transmittance measurement is then conducted. Finally, magnetic behavior was determined at room temperature and 5 K using a vibrating sample magnetometer (VSM) and a superconducting quantum interference device (SQUID) magnetometer (Quantum Design, MPMS-7) under applied magnetic fields up to 5 T.

3. Results and discussions

3.1. Phase analysis

X-ray diffraction (XRD) analysis was conducted to examine the crystal structure of the prepared samples. The X-ray diffraction patterns for $CoFe_{2-x}Co_xO_4$ nanoparticles (where x = 0.0, 0.1, 0.2, 0.3, 0.4, 0.5, and 0.6) are illustrated in Fig. 1. The patterns and corresponding data reveal that all samples exhibit a cubic spinel structure with the $Fd\bar{3}m$ space group. The XRD patterns feature notable peaks indexed as (220), (311), (222), (400), (422), (511), and (440), characteristic of the cubic spinel structure. These peaks were consistently identified as spinel ferrites according to JCPDS card no. 001-1121. Additionally, Fig. 1 shows that samples with higher cobalt concentrations (x = 0.4 and 0.6) contain a minor presence of a secondary phase (CoO). The shifting of the peaks toward lower angles does not display a distinct trend, indicating that the lattice parameters of the samples vary without a consistent pattern. The crystallite sizes were estimated from the XRD spectra using the Debye-Scherrer formula, represented by the following equation [16]:

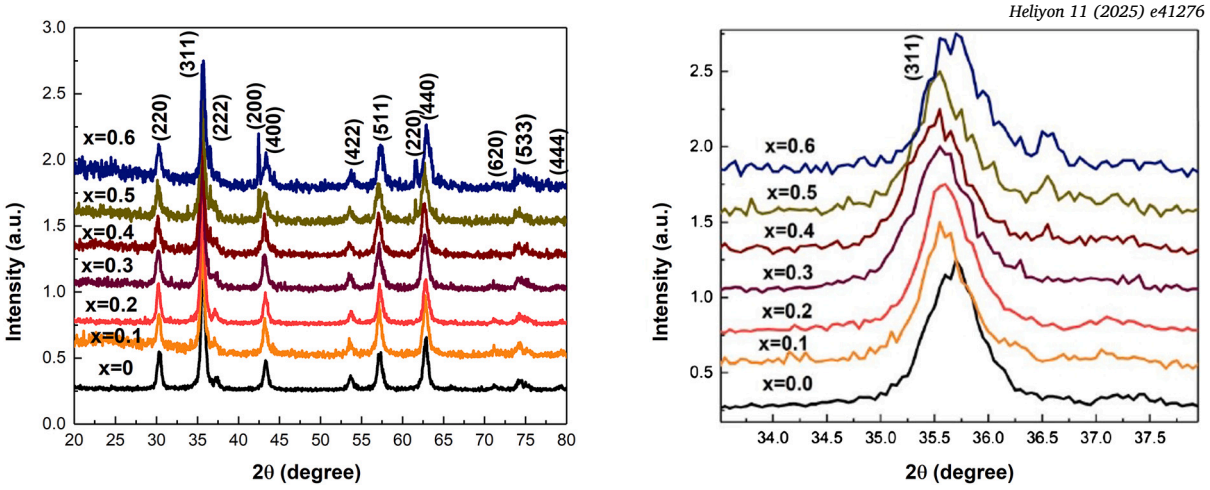

Fig. 1. XRD patterns of $CoFe_{2-x}Co_xO_4$ (x = 0.0, 0.1, 0.2, 0.3, 0.4, 0.5 and 0.6) nanoparticles and magnified section of (311) indicating peak shits.

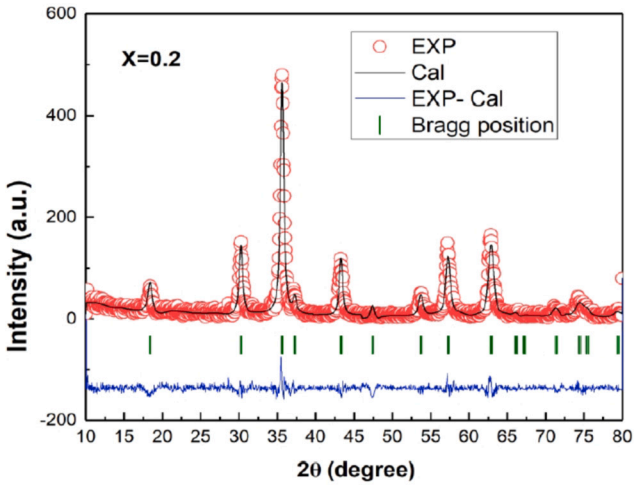

Fig. 2. X-ray patterns for the $CoFe_{1.8}Co_{0.2}O_4$ ferrite nanoparticle refined by FULLPROF program.

$$D = \frac{0.9\lambda}{\beta cos\theta} \tag{1}$$

In this formula, λ represents the wavelength of the X-ray radiation, β denotes the full width at half maximum (FWHM) of the strongest diffraction peak, and θ is the angle of diffraction. Additionally, the relationship between the lattice parameter and volume in a cubic crystal structure is described by equations (2) and (3). In these equations, a refers to the lattice parameter, (h, k, l) are the Miller indices, and d_{hkl} signifies the interplanar distance [17].

$$a = d_{hkl}(h^2 + k^2 + l^2)^{\frac{1}{2}} \tag{2}$$

$$V = a^3 \tag{3}$$

To gain further insights into the samples, Rietveld refinements of the XRD data were performed using the FULLPROF program. The satisfactory agreement between the fitted results and experimental data is illustrated in Fig. 2, which represents the typical case for the sample with x = 0.2.

The findings related to the XRD and the Rietveld refinement parameters are summarized in Table 1. The parameters R_{wp}, R_{exp} and Sig represent the weighted residual error, expected error, and goodness of fit (where $sig = \frac{R_{wp}}{R_{exp}}$), respectively. A slight increase in the lattice parameters observed from the XRD patterns for x = 0 to x = 0.3 can be attributed to the variance in ionic radii between Co^{+2}, Co^{+3} and Fe^{+3} ions. Additionally, at higher substitution levels (x≥0.4), the presence of impurities in the samples may contribute to a decrease in the lattice parameter.

It is crucial to understand that the distribution of cations between tetrahedral and octahedral sites is primarily influenced by the overall energy of the crystal, which is affected by factors such as ionic radius, Coulomb energy, crystal field effects, and the

Table 1
XRD pattern refinements using Rietveld method for $CoFe_{2-x}Co_xO_4$.

x (at.%)	a_{XRD} (Å)	$a_{Rietveld}$ (Å)	D (Å)	sig	R_{wp}	R_{exp}
0.0	8.33	8.39	17.95	1.12	23.13	20.54
0.1	8.34	8.38	17.53	1.23	23.26	18.82
0.2	8.38	8.36	17.55	1.10	22.33	20.21
0.3	8.38	8.38	17.33	1.09	21.98	20.04
0.4	8.37	8.39	15.33	1.17	22.33	18.96
0.5	8.32	8.40	16.75	1.20	24.36	20.27
0.6	8.27	8.35	14.81	1.17	23.74	20.14

Table 2
Theoretical values of the lattice parameter, the ionic radii and cation distortion of A and B sites.

x (at.%)	a_{th} (Å)	r_A (Å)	r_B (Å)	cation distortion (A site)	cation distortion (B site)
0.0	8.31	0.4927	0.7509	$(Co^{2+}_{0.03}Fe^{3+}_{0.97})$	$(Co^{2+}_{0.97}Fe^{3+}_{1.03})$
0.1	8.32	0.4984	0.7488	$(Co^{2+}_{0.09}(Co^{3+}_{0.01}Fe^{3+}_{0.9})$	$(Co^{2+}_{0.97}Co^{3+}_{0.03}Fe^{3+}_{1.0})$
0.2	8.32	0.5011	0.7471	$(Co^{2+}_{0.12}Co^{3+}_{0.01}Fe^{3+}_{0.87})$	$(Co^{2+}_{1.05}Co^{3+}_{0.02}Fe^{3+}_{0.93})$
0.3	8.33	0.5077	0.7469	$(Co^{2+}_{0.19}Co^{3+}_{0.02}Fe^{3+}_{0.79})$	$(Co^{2+}_{1.08}Co^{3+}_{0.01}Fe^{3+}_{0.91})$
0.4	8.25	0.4951	0.7277	$(Co^{2+}_{0.01}Co^{3+}_{0.14}Fe^{3+}_{0.85})$	$(Co^{2+}_{0.88}Co^{3+}_{0.37}Fe^{3+}_{0.75})$
0.5	8.23	0.4951	0.7199	$(Co^{2+}_{0.01}Co^{3+}_{0.14}Fe^{3+}_{0.85})$	$(Co^{2+}_{0.86}Co^{3+}_{0.49}Fe^{3+}_{0.65})$
0.6	8.21	0.4951	0.7121	$(Co^{2+}_{0.01}Co^{3+}_{0.14}Fe^{3+}_{0.85})$	$(Co^{2+}_{0.84}Co^{3+}_{0.61}Fe^{3+}_{0.55})$

arrangement of cations [19]. The distribution of cations over octahedral and tetrahedral sites can be represented as: $(Co^{2+}_{x}Fe^{3+}_{1-x})_A$ $(Co^{2+}_{1-x}Fe^{3+}_{1+x})_B$ O_4 The ionic radii for tetrahedral and octahedral coordination can be calculated using the following equation [20]:

$$r_A = \sum_i r_i \alpha_i \qquad r_B = \frac{1}{2}\sum_i r_i \alpha_i \tag{4}$$

In this context, α represents the quantity of the substituted ion, while r_i denotes the ionic radii at the A and B sites, respectively. The ionic radii are as follows: (0.58 Å, 0.72 Å) [21,22] for Co^{2+}, (0.52 Å, 0.64 Å) [22] for Co^{3+} and (0.49 Å, 0.78 Å) [23,24] for Fe^{3+}. It is important to note that there is a relationship exist between the ionic radius and the lattice parameter. The lattice parameter can be theoretically calculated using the following equation [20]:

$$a_{th} = \frac{8}{3\sqrt{3}}[(r_A + R_0) + \sqrt{3}(r_B + R_0)] \tag{5}$$

Here, R_0 represents the radius of the oxygen ions, with a value of $R_0 = 1.32$ Å. The theoretical values for the lattice parameter, ionic radii, and cation distortion for both tetrahedral (A-site) and octahedral (B-site) ions are summarized in Table 2. As mentioned earlier, the observed slight increase in the lattice parameter for $x < 0.3$, followed by a subsequent decrease for $x > 0.3$, is likely attributed to the distribution of Co^{2+}, Co^{3+}, and Fe^{3+} ions with different ionic radii at the A and B sites, as detailed in Table 2. These findings demonstrate a strong correlation with the experimental results obtained, further emphasizing the influence of ionic distribution on the lattice structure. Using the experimental data for the lattice constant and the oxygen position parameter (expressed as $u = (r_A + R_0)\frac{1}{a\sqrt{3}} + \frac{1}{4}$), we conducted calculations to determine the hopping length between the magnetic ions in the tetrahedral (A) site and the octahedral (B) site. We also calculated the bond lengths for the tetrahedral (denoted as d_{AX}) and octahedral (denoted as d_{BX}) sites. Furthermore, we estimated the tetrahedral edge length (d_{AXE}), which corresponds to the closest distance between anions at the tetrahedral sites, along with the shared and unshared octahedral edges (d_{BXE} and d_{BXEU}, respectively. Please refer to equations (6) through (12) for more details [25]. The results of these calculations are presented in Table 3.

$$L_A = 0.25a\sqrt{3} \tag{6}$$

$$L_B = 0.25a\sqrt{2} \tag{7}$$

$$d_{AX} = 1.732a(u - 0.25) \tag{8}$$

$$d_{BX} = a(3u^2 - 2.75u + 0.6719)^{\frac{1}{2}} \tag{9}$$

$$d_{AXE} = 1.4142(2u - 0.5) \tag{10}$$

$$d_{BXE} = 1.4142a(1 - 2u) \tag{11}$$

$$d_{BXEU} = a(4u^2 - 3u + 0.6875)^{\frac{1}{2}} \tag{12}$$

As the substitution of Co^{3+} increases, the hopping length between the magnetic ions in the tetrahedral (A) site and the octahedral (B)

Table 3
Structural parameter values of hopping length (L_A, L_B), values of bond lengths of tetrahedral (d_{AX}) and octahedral (d_{BX}), tetrahedral edge (d_{AXE}) sites, shared and unshared octahedral edges (d_{BXE} and d_{BXEU}) of $CoFe_{2-x}Co_xO_4$ nanoparticles.

	$x = 0.0$	$x = 0.1$	$x = 0.2$	$x = 0.3$	$x = 0.4$	$x = 0.5$	$x = 0.6$
L_A (Å)	3.5983	3.6027	3.6027	3.6070	3.5723	3.5636	3.5550
L_B (Å)	2.9380	2.9416	2.9416	2.9451	2.9168	2.9097	2.9026
d_{AX} (Å)	1.8127	1.8183	1.8210	1.8276	1.8150	1.8150	1.8150
d_{BX} (Å)	2.0701	2.0706	2.0691	2.0690	2.0463	2.0388	2.0314
d_{AXE} (Å)	2.9601	2.9694	2.9738	2.9846	2.9640	2.9640	2.9640
d_{BXE} (Å)	2.7970	2.8003	2.8003	2.8037	2.7767	2.7700	2.7633
d_{BXEU} (Å)	2.9397	2.9433	2.2493	2.9468	2.9184	2.9114	2.9043

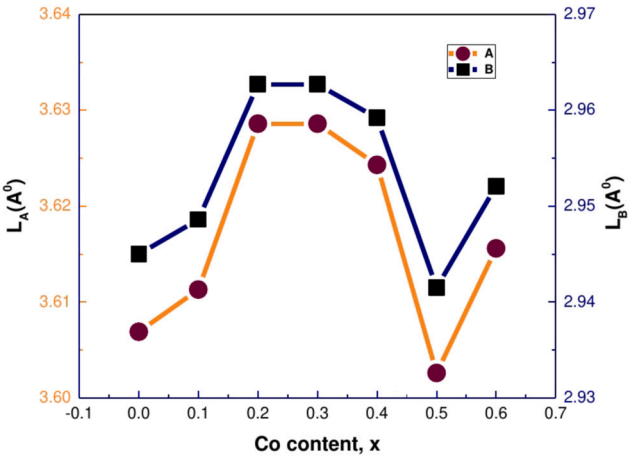

Fig. 3. The behavior of the values hopping length between the magnetic ions in the tetrahedral (A) site and the octahedral (B) site.

Table 4
The formulas for calculating the cation-cation (Me-Me) and cation-anion (Me-O) distances, along with the bond angles.

Distances Me-O	Distances Me-Me	Bond angle
$p = a(\frac{5}{8} - u)$	$b = \sqrt{2}\frac{a}{4}$	$\theta_1 = cos^{-1}\frac{(p^2+q^2-c^2)}{2pq}$
$q = a\sqrt{3}(u - \frac{1}{4})$	$c = \sqrt{11}\frac{a}{8}$	$\theta_2 = cos^{-1}\frac{(p^2+r^2-e^2)}{2pr}$
$r = a\sqrt{11}(u - \frac{1}{4})$	$d = \sqrt{3}\frac{a}{4}$	$\theta_3 = cos^{-1}\frac{(2p^2-b^2)}{2p^2}$
$s = a\sqrt{3}(\frac{u}{3} + \frac{1}{8})$	$e = \sqrt{3}\frac{3a}{8}$	$\theta_4 = cos^{-1}\frac{(p^2+s^2-f^2)}{2ps}$
	$f = \sqrt{6}\frac{a}{4}$	$\theta_5 = cos^{-1}\frac{(r^2+q^2-d^2)}{2qr}$

site varies, as illustrated in Fig. 3. The distribution of cations between the tetrahedral and octahedral sites notably affects both bond lengths and edge dimensions. With increased cobalt substitution, bond lengths in both sites also rise. Specifically, the bond lengths at the tetrahedral (d_{AX}) and octahedral (d_{BX}) sites are directly correlated with the lattice parameter, thereby making the observed increase in bond lengths in both positions expected.

We also calculated the interaction distances and angles between the metal ions and oxygen in all samples based on the XRD results. These parameters are summarized in Table 4, where p, q, r, and s represent the interaction distances between metal cations and oxygen anions. Additionally, b, c, d, e, and f denote the interaction distances when only metal ions are involved in the chemical bonds [16]. Furthermore, Fig. 4 presents a diagram illustrating the angles θ_1 to θ_5, which depict the arrangement of ions in both octahedral and tetrahedral configurations. The obtained values of these quantities are documented in Table 5 and Table 6. The experimental analysis reveals that the intrinsic distances increase gradually with the increment of cobalt substitution. In an undistorted spinel structure, the A-O-B angles are approximately 125° and 154°. The B-O-B angles are around 90° and 125°. Additionally, for the A-A configuration, the angle is approximately 80° [26]. The results indicate that the distortion caused by cobalt doping in $CoFe_2O_4$ has influenced the angles between interactions and led to a reduction in θ_5.

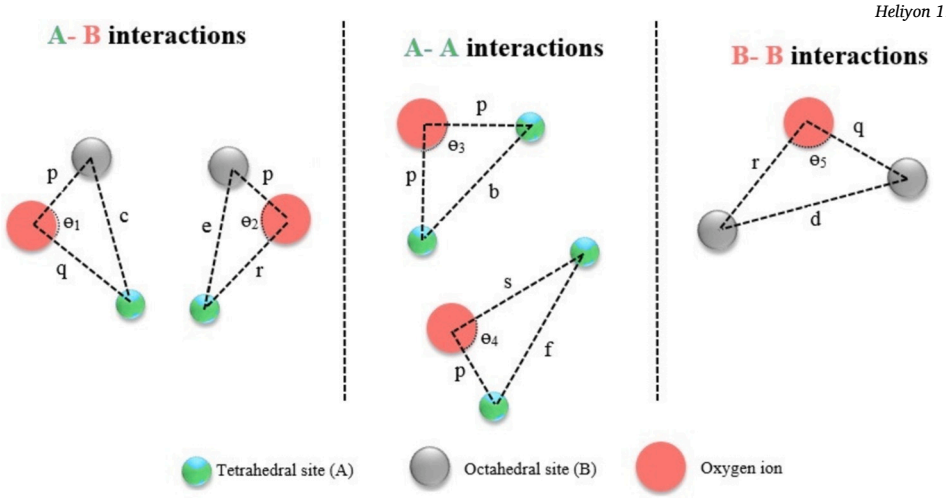

Fig. 4. Interionic distances and angles in the spinel structures.

Table 5
The estimated distances between cation-cation and cation-anion at the tetrahedral (A) site and octahedral (B) site.

x (at.%)	p	q	r	s	b	c	d	e	f
0.0	2.0775	1.8121	3.4700	3.609	2.9450	3.4534	3.6069	5.4104	5.1010
0.1	2.0741	1.8244	3.4935	3.6175	2.9486	3.4575	3.6113	5.4169	5.1071
0.2	2.0882	1.8259	3.4963	3.6325	2.9627	3.4741	3.6286	5.4429	5.1316
0.3	2.0857	1.8302	3.5047	3.6339	2.9627	3.4741	3.6286	5.4429	5.1316
0.4	2.0782	1.8368	3.5172	3.6325	2.9592	3.4700	3.6243	5.4364	5.1255
0.5	2.0641	1.8287	3.5017	3.6117	2.9415	3.4492	3.6026	5.4039	5.4039
0.6	2.0766	1.8266	3.4977	3.6219	2.9521	3.4617	3.6156	5.4234	5.1133

Table 6
Angles between cation-cation and cation-anion at tetrahedral (A) site and octahedral (B) site.

x (at.%)	θ_1	θ_2	θ_3	θ_4	θ_5
0.0	125.070	153.619	90.276	125.329	79.395
0.1	124.844	152.346	90.600	125.405	78.727
0.2	125.005	153.249	90.368	125.350	79.203
0.3	124.908	152.703	90.507	125.383	78.917
0.4	124.715	151.643	90.787	125.448	78.350
0.5	124.650	151.298	90.880	125.470	78.163
0.6	124.844	152.346	90.600	125.405	78.727

3.2. Morphology of nanoparticles

An analysis of the surface morphology and grain size of $CoFe_{2-x}Co_xO_4$ samples was performed using Field Emission Scanning Electron Microscopy (FESEM). As shown in Fig. 5, the FESEM micrographs indicate that the nanoparticles are predominantly spherical, with a grain size within the range of 50 to 90 nm. Furthermore, the inherent magnetism of the particles contributes to their tendency to aggregate, resulting in an increase in grain size with greater substitution of Co^{3+}.

3.3. Magnetic analysis

Fig. 6 displays the measured magnetization (M) as a function of the applied field (H) for $CoFe_{2-x}Co_xO_4$ samples at room temperature, with the corresponding magnetic parameters summarized in Table 7. Initially, the saturation magnetization (M_S) values increase with higher levels of Co^{3+} doping. This enhancement in M_S can be attributed to changes in cation distribution, as shown in Table 2. $CoFe_2O_4$ exhibits an inverse spinel structure in which divalent Co^{2+} ions occupy the octahedral sites, while Fe^{3+} cations are located in both tetrahedral and octahedral sites. The net magnetic moment of the $CoFe_2O_4$ unit cell primarily results from the difference between the magnetic moments in the tetrahedral (B) and octahedral (A) sites. As Co^{3+} ions (with a smaller magnetic moment of $4\mu_B$) replace Fe^{3+} cations (which have a larger magnetic moment of 5μB) at the A site, the overall magnetization increases for

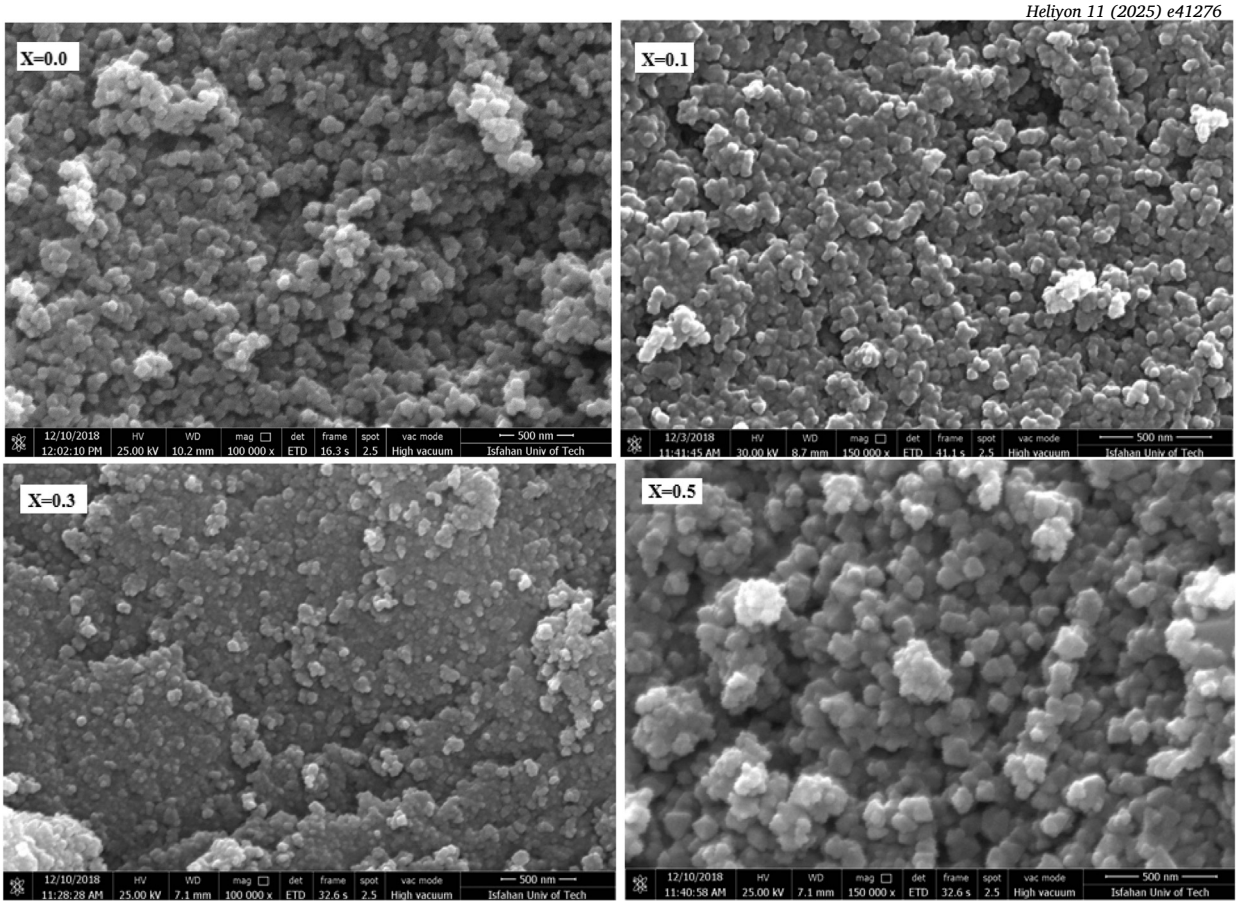

Fig. 5. FE-SEM of $CoFe_{2-x}Co_xO_4$ (x = 0.0, 0.1, 0.3 and 0.5) nanoparticles.

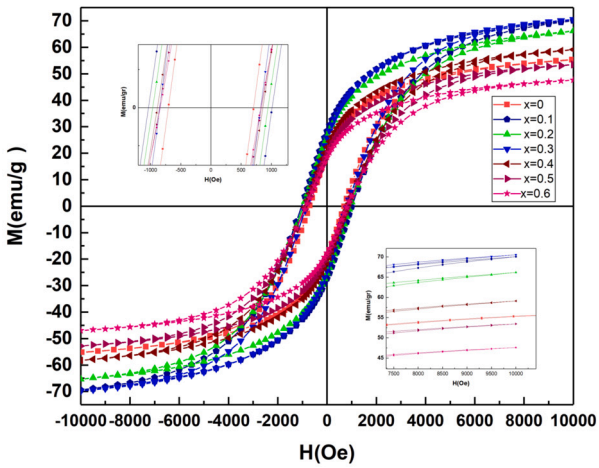

Fig. 6. The hysteresis loops of $CoFe_{2-x}Co_xO_4$ (x = 0.0, 0.1, 0.2, 0.3, 0.4, 0.5 and 0.6) ferrite nanoparticles at 300 K.

samples with x < 0.3. However, at higher doping levels (x > 0.3), the increased presence of Co^{2+} ions at the A sites, the replacement of Fe^{3+} with Co^{3+} at the B sites, and the incorporation of impurities lead to a reduction in saturation magnetization.

Additionally, the coercivity (H_C) exhibits a decreasing trend with increasing Co concentration, reaching a minimum value at x = 0.3, before rising again with further increases in doping content. This behavior can be explained by particle size; the increase in H_C with particle size indicates of single-domain particle characteristics, as previously reported [27]. According to Néel's law, the magnetic moment can be calculated from the cation distribution by determining the difference between the total magnetic moments of the B sites and A sites. This relationship is expressed mathematically as: $n^B_{cal} = M_B\text{-}M_A$. Here n^B_{cal} is the theoretical value of the

Table 7
Coercive field (H_C), remanent magnetization (M_r), saturation magnetization (M_S) and remanence ratios (R) values extracted from M - H loops.

x (at.%)	H_C(Oe)	M_r (emu/g)	M_S (emu/g)	$R = \frac{M_r}{M_S}$
0.0	704.78	18.99	55.33	0.34
0.1	1024.66	27.86	70.06	0.39
0.2	953.33	25.94	66.17	0.39
0.3	834.62	25.10	70.52	0.36
0.4	872.66	21.83	59.12	0.37
0.5	844.77	19.46	53.45	0.37
0.6	829.89	18.06	47.61	0.38

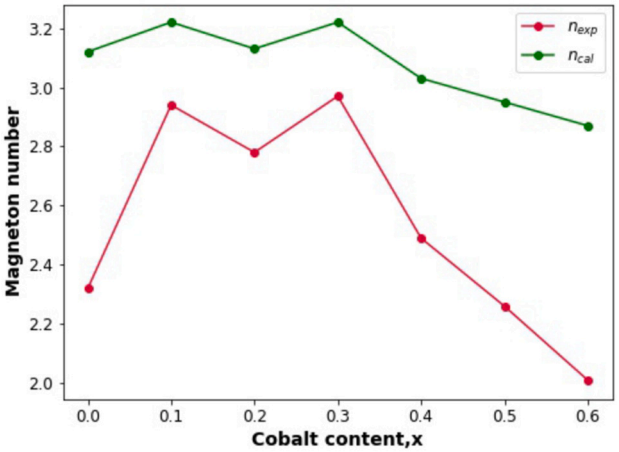

Fig. 7. Variation of experimental and calculated magnetic moment with composition x of $CoFe_{2-x}Co_xO_4$ (x = 0.0, 0.1, 0.2, 0.3, 0.4, 0.5 and 0.6) nanoparticles.

magnetic moment, M_B represents the magnetic moment of the B sites, and M_A is the magnetic moment of the A sites. Additionally, the magnetic moment can be derived from experimental data using the following relationship, where M_w denotes the molecular weight of each sample:

$$n^B_{exp} = \frac{M_w \times M_s}{5585} \tag{13}$$

The illustration in Fig. 7 shows the variations in magnetic moment as a function of cobalt composition (x), comparing both experimental and calculated values. The figure emphasizes a strong correlation between the experimental observations and the theoretical predictions, indicating that the cation distribution and Néel's law effectively describe the magnetic behavior of the cobalt-doped ferrites. This alignment indicates that the theoretical models effectively capture the fundamental magnetic properties of the material as the cobalt content varies.

3.4. Optical characterization

The optical absorption spectra of the samples were obtained using UV-Vis spectrophotometry. Fig. 8 illustrates the absorption spectra of all the samples. The synthesized samples exhibit absorption peaks at the ultraviolet and visible region. A strong absorption peak is observed around 300 nm wavelength in the spectrum of $CoFe_{2-x}Co_xO_4$ nanoparticles.

The optical band gap (E_g) of $CoFe_{2-x}Co_xO_4$ nanoparticles was determined from the absorption spectra using the following equation:

$$\alpha h\nu = A(h\nu - E_g)^n \tag{14}$$

In this context, α represents the absorption coefficient, h is Planck's constant, A is a constant, and E_g is the energy band gap. The parameter n indicates the type of optical transition and is limited to values of $\frac{1}{2}$, 2, $\frac{3}{2}$, and 3, which correspond to direct electronic transitions (direct band gap), indirect electronic transitions (indirect band gap), forbidden direct transitions, and forbidden indirect transitions, respectively [8]. To analyze the band edges, the Tauc equation is applied for direct band transitions. By plotting $((\alpha h\nu)^2)$ versus photon energy (see Fig. 9), the linear segment of the resulting curve can be extended to the energy axis. The point of intersection indicates the approximate value of (E_g) [8]. The energy band gap of all samples was calculated using Bras' effective mass model. In this model, the energy band gap E_g can be expressed as a function of particle size [28]:

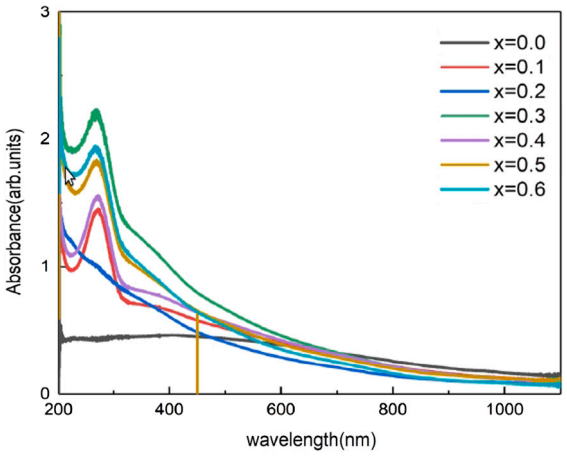

Fig. 8. UV-Vis spectra of $CoFe_{2-x}Co_xO_4$ nanoparticles.

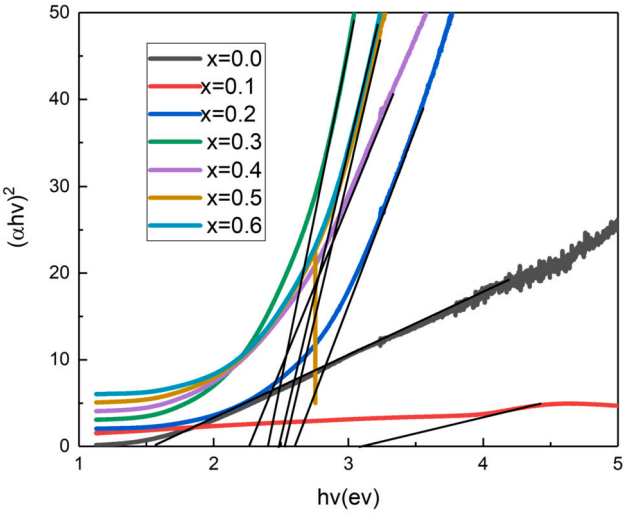

Fig. 9. Plots of $(\alpha h\nu)^2$ as a function of photon energy $(h\nu)$ for all samples.

Table 8
Energy band gap for $CoFe_{2-x}Co_xO_4$ samples.

	$x = 0.0$	$x = 0.1$	$x = 0.2$	$x = 0.3$	$x = 0.4$	$x = 0.5$	$x = 0.6$
E_g(eV)	1.7	3.2	2.7	2.4	2.3	2.6	2.5

$$E_g^{nano} \cong E_g^{bulk} \frac{h^2}{8m_0r^2}\left(\frac{1}{m_e} + \frac{1}{m_h}\right) + \frac{1.8e^2}{4\pi\varepsilon\varepsilon_0 r} \tag{15}$$

Table 8 presents the values for the direct band gaps. It is noted that the band gap ranges from 1.7 to 3.2 eV for varying concentrations of Co^{3+}, with the maximum band gap occurring at x = 0.1. The band gap obtained for the sample with x = 0.0 aligns well with the previously reported value [29]. Various factors, including the cation distribution, presence of impurities, crystallite size, lattice parameter, and surface/interface effects, significantly influence the band gap [30].

4. Effect of annealing temperature

4.1. Effect of annealing temperature on structural properties

To eliminate impurities and investigate the effect of annealing temperature on the structural and magnetic properties of $CoFe_{2-x}Co_xO_4$ nanoparticles, samples were sintered in air at 1000 °C for 3 hours. Fig. 10 presents the XRD pattern of the $CoFe_{2-x}Co_xO_4$ nanoparticles after annealing at 1000 °C. Based on the standard $CoFe_2O_4$ powder diffraction data (JCPDS card no. 391346), all observed peaks correspond to pure cubic phase nanoparticles with a space group of $Fd\bar{3}m$. From the XRD spectrum, the

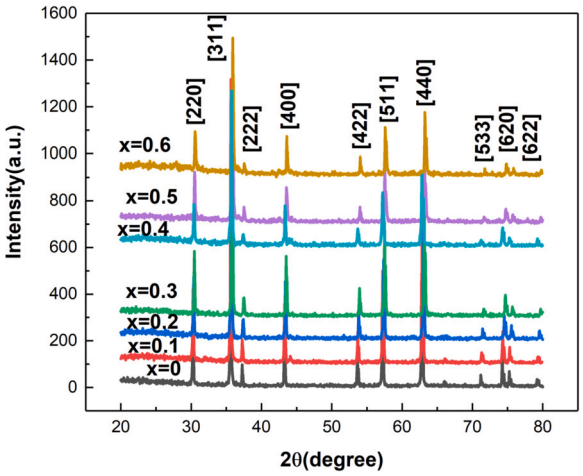

Fig. 10. XRD patterns of the $CoFe_{2-x}Co_xO_4$ annealed at 1000 °C.

Table 9
Lattice parameter, crystalline size, unit cell volume and hopping length for $CoFe_{2-x}Co_xO_4$ annealed at 1000 °C.

	$x = 0.0$	$x = 0.1$	$x = 0.2$	$x = 0.3$	$x = 0.4$	$x = 0.5$	$x = 0.6$
a (Å)	8.37	8.36	8.33	8.33	8.30	8.29	8.27
D (nm)	51	45	49	44	50	54	44
V (Å^3)	586.37	584.27	578.00	575.93	571.79	569.72	565.60
L_A (Å)	3.6243	3.6199	3.6069	3.6026	3.5940	3.5896	3.5810
L_B (Å)	2.9592	2.9557	2.9450	2.9415	2.9344	2.9309	2.9238

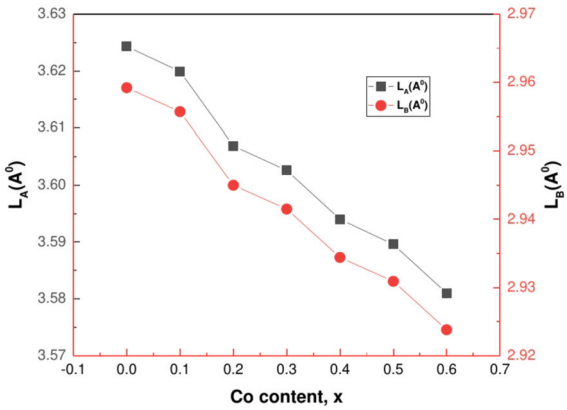

Fig. 11. The trend of L_A and L_B as functions of the Co content (x) in $CoFe_{2-x}Co_xO_4$ samples annealed at 1000 °C.

lattice parameter (as described in Equation (2)), crystallite size (according to Equation (1)), and unit cell volume (as per Equation (3)) were determined and are summarized in Table 9.

The slight variation in the lattice parameter with increasing Co^{3+} substitution can be attributed to the differences in the ionic radii of Fe^{3+} and Co^{3+}. Specifically, the ionic radius of Fe^{3+} is 0.49 Å at the tetrahedral (A-sites) and 0.64 Å at the octahedral (B-sites). In comparison, the ionic radius of Co^{3+} is 0.52 Å at tetrahedral sites and 0.61 Å at octahedral sites [18]. Consequently, the gradual doping of Co^{3+} cations leads to a shrinkage of the lattice. The results indicate that during the Co substitution process, Co^{3+} ions preferentially replace Fe^{3+} in the B site. From the obtained lattice parameters, we calculated the hopping length between the magnetic ions in the tetrahedral (A) site and the octahedral (B) site. It was observed that the associated parameters decrease with increasing Co^{3+} ion substitution (see Fig. 11). This suggests that Co^{3+} ions show a preference for occupying the octahedral B sites. The theoretical values for the lattice parameter, ionic radii, and cation distortion for both tetrahedral (A-site) and octahedral (B-site) ions are summarized in Table 10. In comparison to the unannealed samples, the width of the diffraction peaks decreased while the intensity increased, suggesting an enhancement in the size of the crystallites. Rietveld refinements of the XRD data were performed using the FULLPROF program, allowing for a detailed analysis of the crystal structure of $CoFe_{2-x}Co_xO_4$. Fig. 12 display a

Table 10
Theoretical values of the lattice parameter, the ionic radii and cation distortion of A and B sites.

x (at.%)	a_{th} (Å)	r_A (Å)	r_B (Å)	cation distortion (A site)	cation distortion (B site)
0.0	8.31	0.4945	0.7515	$(Co^{2+}_{0.05}Fe^{3+}_{0.95})$	$(Co^{2+}_{0.95}Fe^{3+}_{1.05})$
0.1	8.30	0.4954	0.7480	$(Co^{2+}_{0.04}(Co^{3+}_{0.06}Fe^{3+}_{0.9})$	$(Co^{2+}_{0.95}Co^{3+}_{0.05}Fe^{3+}_{1.0})$
0.2	8.28	0.4954	0.7398	$(Co^{2+}_{0.04}Co^{3+}_{0.06}Fe^{3+}_{0.90})$	$(Co^{2+}_{0.92}Co^{3+}_{0.18}Fe^{3+}_{0.90})$
0.3	8.26	0.4954	0.7320	$(Co^{2+}_{0.04}Co^{3+}_{0.06}Fe^{3+}_{0.90})$	$(Co^{2+}_{0.90}Co^{3+}_{0.3}Fe^{3+}_{0.80})$
0.4	8.24	0.4954	0.7246	$(Co^{2+}_{0.04}Co^{3+}_{0.06}Fe^{3+}_{0.90})$	$(Co^{2+}_{0.89}Co^{3+}_{0.41}Fe^{3+}_{0.70})$
0.5	8.22	0.4954	0.7168	$(Co^{2+}_{0.01}Co^{3+}_{0.14}Fe^{3+}_{0.85})$	$(Co^{2+}_{0.87}Co^{3+}_{0.53}Fe^{3+}_{0.60})$
0.6	8.20	0.4954	0.7090	$(Co^{2+}_{0.04}Co^{3+}_{0.06}Fe^{3+}_{0.9})$	$(Co^{2+}_{0.85}Co^{3+}_{0.65}Fe^{3+}_{0.50})$

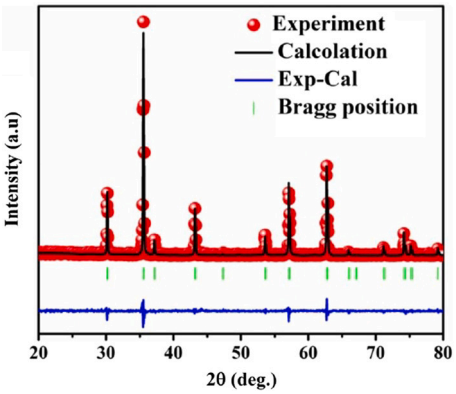

Fig. 12. Rietveld analysis for the $CoFe_{1.8}Co_{0.2}O_4$ sample annealed at 1000 °C.

Table 11
XRD pattern refinements using Rietveld method for $CoFe_{2-x}Co_xO_4$ annealed at 1000 °C.

	$x = 0.0$	$x = 0.1$	$x = 0.2$	$x = 0.3$	$x = 0.4$	$x = 0.5$	$x = 0.6$
a (Å)	8.38	8.36	8.35	8.34	8.34	8.33	8.31
Sig	1.48	1.80	1.70	1.70	1.21	1.49	1.32
R_{wp}	33.1721	37.4548	34.0263	36.0732	25.4146	28.3241	27.3432
R_{exp}	22.2984	20.7001	19.9979	21.1985	20.8644	18.9967	20.5683

typical Rietveld analysis for x = 0.2 sample, showing the fitted profile alongside the observed data, as well as the difference plot. The estimated values of the Rietveld refinement parameters are summarized in Table 11.

4.2. Magnetic properties

Fig. 13 displays the magnetization loops for $CoFe_{2-x}Co_xO_4$ nanoparticles annealed at 1000°. The magnetization was analyzed using Superconducting Quantum Interference Device (SQUID) magnetometry at 5 and 300 K. The results illustrate the magnetic behavior of the nanoparticles under varying magnetic fields. The values of saturation magnetization (M_S), coercive field (H_C), remanence magnetization (M_r), and squareness ratio (R) are summarized in Table 12. The observations suggest that the applied magnetic field is insufficient for fully aligning the spins in the direction of the field at low temperatures, suggesting notable anisotropy or other magnetic interactions within the nanoparticles. The variation of saturation magnetization (M_S) and coercive field (H_C) with Co^{+3} substitution at 5 K and 300 K is illustrated in Fig. 14 and Fig. 15, respectively. At both temperatures, a noticeable decreasing trend in magnetization is observed with increased Co^{+3} substitution. This decrease in magnetization can be attributed to the distribution of cations across the various sublattices, as previously discussed for the unannealed samples. At 300 K, the coercive field (H_C) exhibited only minor changes; however, its behavior at 5 K was inconsistent. The coercive field of ferrite nanoparticles is affected by several factors, including internal microstress that distorts the lattice structure, as well as variations in particle size and electronic configurations [31].

It is noted that after annealing, the saturation magnetization and coercive field increase significantly due to several factors. First, annealing promotes the crystallization of the material, which can lead to improved structural order and reduced internal defects. This enhancement in crystallinity facilitates better alignment of magnetic moments within the material, resulting in higher saturation magnetization.

Additionally, annealing can induce grain growth, which may diminish magnetostatic interactions between nanoparticles and allow for greater coherence of magnetic domains. This alignment helps in achieving a more uniform and stronger net magnetization. Another

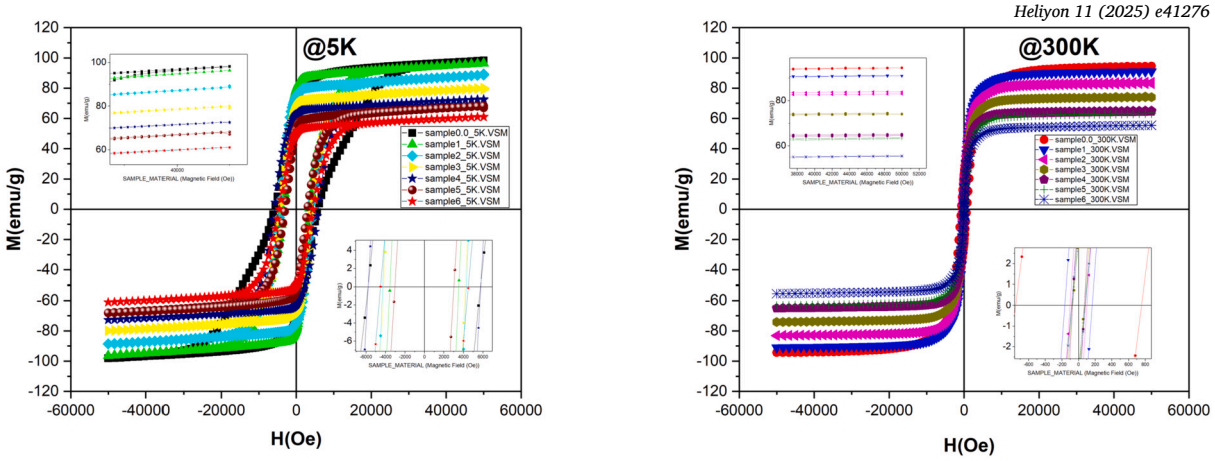

Fig. 13. VSM of $CoFe_{2-x}Co_xO_4$ at 5 and 300 K.

Table 12
Saturation magnetization (M_S), coercive force (H_C), remanent magnetization (M_r), and anisotropy constant (K) as a function of Sm content (x) measured at temperatures 5 K (a), and 300 K (b).

x (at.%)	H_C(Oe)	M_r (emu/g)	M_S (emu/g)	$R = \frac{M_r}{M_S}$
T = 5 K				
0.0	5764.13	69.30	98.20	0.70
0.1	3534.00	78.51	96.30	0.81
0.2	4281.00	74.33	88.80	0.83
0.3	4173.09	66.91	79.68	0.84
0.4	5781.09	6242	72.69	0.85
0.5	3031.59	53.35	67.95	0.79
0.6	4508.85	49.92	61.04	0.81
T = 300 K				
0.0	768.40	23.12	94.48	0.24
0.1	165.36	8.62	90.94	0.09
0.2	102.30	6.07	83.30	0.07
0.3	69.21	3.39	74.10	0.04
0.4	70.95	5.32	64.88	0.08
0.5	76.74	3.09	63.36	0.04
0.6	83.36	3.86	55.40	0.07

contributing factor is the redistribution of cations during the annealing process. This can optimize the cation distribution among the octahedral and tetrahedral sites, increasing the overall magnetic moment of the material according to Néel's model. Finally, the reduction of internal microstress and defects resulting from the annealing treatment can further improve the stability of the magnetic domains, contributing to an increase in the coercive field (H_C). Overall, these changes result in enhanced magnetic properties of the samples after annealing.

5. Conclusions

In conclusion, this study successfully synthesized $CoFe_{2-x}Co_xO_4$ nanoparticles using hydrothermal methods, revealing significant insights into the structural, morphological, optical, and magnetic properties of these materials influenced by cobalt substitution. X-ray diffraction analysis confirmed the formation of a cubic spinel structure, while FE-SEM revealed average grain sizes ranging from 50 nm and 90 nm, indicating the successful cultivation of nanoparticles.

The investigation of optical properties showed a notable increase in the band gap of Co^{+3}-doped samples from 1.7 eV to 2.5 eV, suggesting potential applicability in optoelectronic devices. Magnetic characterization demonstrated a decrease in saturation magnetization with rising Co^{+3} content at both 5 K and 300 K, driven by the migration of Co^{+2} ions to the A site and the substitution of Fe^{+3} ions in the B site, which have important implications for magnetic performance in various applications. Finally, the effects of annealing were considered, highlighting its role in optimizing the structural and magnetic properties of the nanoparticles. Overall, the findings of this study contribute to the understanding of how cobalt doping can tailor the properties of $CoFe_2O_4$ nanoparticles, paving the way for their potential applications in biomedical, magnetic, and electronic fields.

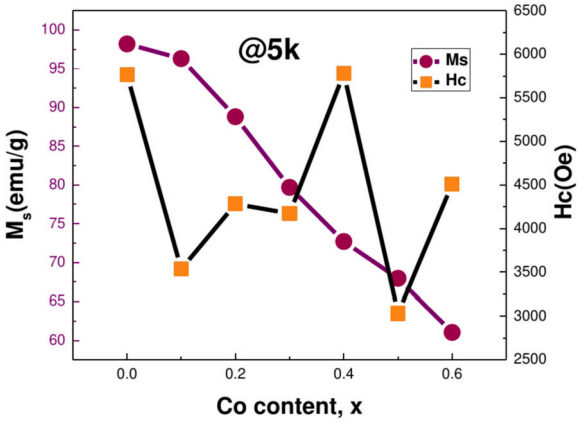

Fig. 14. The total trend of M_S and H_C as functions of the co content (x) in 5 K.

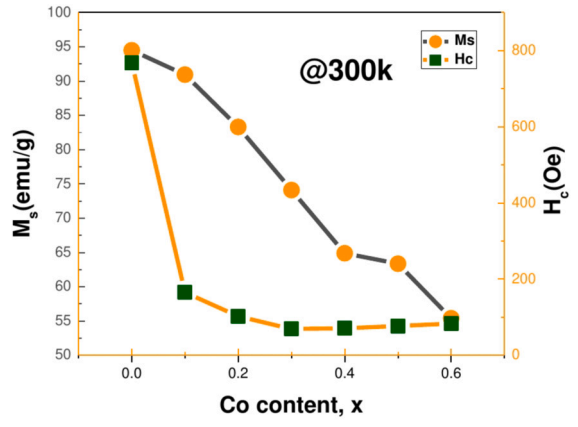

Fig. 15. The total trend of M_S and H_C as functions of the co content (x) in 300 K.

CRediT authorship contribution statement

Z. Mosleh: Writing – review & editing, Writing – original draft, Software, Formal analysis, Data curation, Conceptualization. **M. Beygmohammadvand:** Investigation. **A. Ghotbi Varzaneh:** Formal analysis. **P. Kameli:** Writing – original draft, Supervision.

Declaration of competing interest

The authors declare that they have no known competing financial interests or personal relationships that could have appeared to influence the work reported in this paper.

References

[1] C. Cheng, J. Dai, Z. Li, W. Feng, Materials 13 (2020) 3860.
[2] S. Khizar, N.M. Ahmad, N. Ahmed, S. Manzoor, M.A. Hamayun, N. Naseer, M.K. Tenório, N. Lebaz, A. Elaissari, Nanomaterials 10 (2020) 2182.
[3] M.A. Ansari, R. Govindasamy, M.Y. Begum, M. Ghazwani, A. Alqahtani, M.N. Alomary, Y.F. Jamous, S.A. Alyahya, S. Asiri, F.A. Khan, et al., Nanotechnol. Rev. 12 (2023) 20230575.
[4] M. Kumar, A. Kumar, A. Singh, A. Anshul, S. Sharma, P.C. Sati, J. Alloys Compd. 896 (2022) 163074.
[5] R. Li, Y. Liao, Y. Dou, D. Wang, G. Li, W. Sun, J. Wu, Z. Lan, Sol. Energy 220 (2021) 400.
[6] K. Wei, H.-X. Huai, B. Zhao, J. Zheng, G.-Q. Gao, X.-Y. Zheng, C.-C. Wang, Sens. Actuators B, Chem. 369 (2022) 132279.
[7] Y. Lu, M. Yousaf, M.N. Akhtar, A. Noor, M. Akbar, M.Y. Shah, S. Yan, F. Wang, Ceram. Int. 48 (2022) 2782.
[8] E. Gharibshahi, B.D. Young, A.S. Bhalla, R. Guo, J. Mater. Sci. Technol. 57 (2020) 180.
[9] M. Al-Gharram, T. AlZoubi, Ceram. Int. 50 (2024) 5473.
[10] K.M. Krishnan, Fundamentals and Applications of Magnetic Materials, Oxford University Press, 2016.
[11] V. Bilovol, M. Sikora, S. Lisníková, J. Żukrowski, K. Berent, M. Gajewska, J. Appl. Phys. 134 (2023).
[12] W. Guijuan, L. Yuanxun, L. Yongcheng, C. Daming, P. Rui, J. Mater. Sci., Mater. Electron. 32 (2021) 13490.
[13] P. Imanipour, S. Hasani, A. Seifoddini, M. Nabiałek, Nanomaterials 12 (2022) 752.
[14] S. Kumar, F. Ahmed, N.M. Shaalan, R. Kumar, A. Alshoaibi, N. Arshi, S. Dalela, F. Sayeed, S. Dwivedi, K. Kumari, Materials 15 (2022) 7955.
[15] D. Zhao, X. Wu, H. Guan, E. Han, J. Supercrit. Fluids 42 (2007) 226.

[16] A.V. Humbe, P.G. Undre, J.S. Kounsalye, N.D. Raskar, V.A. Mane, B.N. Dole, J. Mater. Sci., Mater. Electron. 35 (2024) 1589.
[17] A. Ghasemi, M. Mousavinia, Ceram. Int. 40 (2014) 2825.
[18] F. Saffari, P. Kameli, M. Rahimi, H. Ahmadvand, H. Salamati, Ceram. Int. 41 (2015) 7352.
[19] N. Liu, P. Du, P. Zhou, R. Tanguturi, Y. Qi, T. Zhang, C. Zhuang, Appl. Surf. Sci. 532 (2020) 147440.
[20] I. Sharifi, H. Shokrollahi, M.M. Doroodmand, R. Safi, J. Magn. Magn. Mater. 324 (2012) 1854.
[21] P. Anantharamaiah, H. Shashanka, R. Kumar, J. Chelvane, B. Sahoo, Mater. Sci. Eng. B 266 (2021) 115080.
[22] B.C. Feng, O. Tegus, T. Ochirkhyag, D. Odkhuu, N. Tsogbadrakh, D. Sangaa, J. Davaasambuu, Solid State Phenom. 310 (2020) 124.
[23] N. Pathak, S.K. Gupta, K. Sanyal, M. Kumar, R. Kadam, V. Natarajan, Dalton Trans. 43 (2014) 9313.
[24] H. Nikmanesh, E. Jaberolansar, P. Kameli, A.G. Varzaneh, Nanotechnology 33 (2022) 275709.
[25] R.S. Yadav, J. Havlica, J. Masilko, L. Kalina, J. Wasserbauer, M. Hajdúchová, V. Enev, I. Kuřitka, Z. Kožáková, J. Magn. Magn. Mater. 399 (2016) 109.
[26] A. Modabberasl, E. Jaberolansar, P. Kameli, H. Nikmanesh, Mater. Chem. Phys. 314 (2024) 128832.
[27] A. Das, K.K. Bestha, P. Bongurala, V. Gorige, Nanotechnology 31 (2020) 335716.
[28] M. Azim, M. Chaudhry, N. Amin, M. Arshad, M. Islam, S. Nosheen, M. Ahmad, H. Anwar, M. Waseem, G. Mustafa, Digest J. Nanomater. Biostruct. 11 (2016) 953.
[29] K. Dubey, S. Dubey, V. Sahu, R.A. Parry, A. Modi, N. Gaur, Appl. Phys. A 128 (2022) 560.
[30] A. Ravindra, M. Chandrika, C. Rajesh, P. Kollu, S. Ju, S. Ramarao, Eur. Phys. J. Plus 134 (2019) 1.
[31] H. Nikmanesh, E. Jaberolansar, P. Kameli, A.G. Varzaneh, M. Mehrabi, M. Rostami, Nanotechnology 33 (2021) 045704.